International Journal of Nanomedicine

Dovepress
open access to scientific and medical research

Open Access Full Text Article

ORIGINAL RESEARCH

Down-Regulation of HSP by Pd-Cu Nanozymes for NIR Light Triggered Mild-Temperature Photothermal Therapy Against Wound Bacterial Infection: In vitro and in vivo Assessments

Yan Zhou[1,2,*], Zekun Zhou[3,*], Xiaojuan Wu[2], Zefeng Wang[2], Wangdan Qi[1], Jing Yang[1], Liming Qing[3], Juyu Tang[3], Le Deng[1]

[1]State Key Laboratory of Developmental Biology of Freshwater Fish, Department of Microbiology, College of Life Science, Hunan Normal University, Changsha, Hunan, People's Republic of China; [2]State Key Laboratory of Chemo/Biosensing and Chemometrics, College of Biology, College of Chemistry and Chemical Engineering, Hunan University, Key Laboratory for Bio-Nanotechnology and Molecule Engineering of Hunan Province, Changsha, Hunan, People's Republic of China; [3]Department of Orthopedics, Hand and Microsurgery, Xiangya Hospital of Central South University, Changsha, Hunan, People's Republic of China

*These authors contributed equally to this work

Correspondence: Le Deng, State Key Laboratory of Developmental Biology of Freshwater Fish, Department of Microbiology, College of Life Science, Hunan Normal University, Changsha, Hunan, People's Republic of China, Email dengle@hunnu.edu.cn; Juyu Tang, Department of Orthopedics, Hand and Microsurgery, Xiangya Hospital of Central South University, Changsha, Hunan, People's Republic of China, Email tangjuyu@csu.edu.cn

Purpose: We aimed to develop an oxidative-stress-activated palladium-copper nanozyme to reduce bacterial's heat sensitivity by down-regulating heat shock proteins to overcome the shortcomings of conventional photothermal antimicrobial therapy and achieve mild photothermal bactericidal efficacy.

Methods: We first synthesized palladium-copper nanozymes (PC-NPs) by hydration and used transmission electron microscopy, X-ray diffraction, and Fourier transform infrared spectroscopy to demonstrate their successful preparation. Their photothermal therapy (PTT) and chemo-dynamic therapy (CDT) activities were then determined by a series of photothermal performance tests and peroxidase-like performance tests, and the destruction of heat shock proteins by reactive oxygen species (ROS) was verified at the protein level by Western Blotting tests, providing a basis for the effective bacteria-killing by the mild-temperature photothermal treatment subsequently applied. We also validated this promising programmed and controlled antimicrobial treatment with palladium-copper nanozymes by in vivo/in vitro antimicrobial assays. A hemolysis assay, MTT cytotoxicity test and histopathological analysis were also performed to assess the in vivo safety of PC-NPs.

Results: In the micro-acidic environment of bacterial infection, PC-NPs showed peroxidase-like activity that broke down the H_2O_2 at the wound into hydroxyl radicals and down-regulated bacterial heat shock proteins. The application of PC-NPs increased bacteria's sensitivity to subsequent photothermal treatment, enabling the elimination of bacteria via mild photothermal treatment.

Conclusion: The programmed synergistic catalytic enhancement of CDT and mild photothermal therapy achieves the most efficient killing of bacteria and their biofilms, which brings future thinking in the relationship between heat shock proteins and oxidative stress damage in bacteria.

Keywords: nanozyme, mild-temperature photothermal therapy, DnaK, reactive oxygen species, ROS, antibiofilm

Introduction

Bacterial infectious diseases pose a continuous threat to human health. Antibiotics have been immediately used to treat bacterial infections[1–3] due to their highly effective bactericidal properties.[4,5] However, the potential problem of drug resistance introduced with the misuse of antibiotics has been defined by the World Health Organization as one of the major sources of risk for global public health security issues.[6–10] To make matters worse, bacteria lurk more deeply on

Received: 25 May 2023
Accepted: 14 August 2023
Published: 22 August 2023

implanted devices or host tissues in resistant forms that form biofilms, and the closer the association between bacteria, the more difficult they are to eradicate.[11–13] This poses a challenge to the growing problem of bacterial resistance, and thus there is an urgent need to find promising approaches to kil bacteria by biofilm.

Photothermal therapy for antibacterial infections (aPTT) is a promising alternative to conventional antibiotic antimicrobial therapy, with its low cost, controllable duration, and high therapeutic efficiency.[14–17] It denatures the proteins or enzymes of bacteria through higher temperatures, inhibiting their internal cellular reactions and ultimately leading to bacterial rupture and efflux of endosomes.[18,19] One impetus for the high temperatures relies on the photothermal agents with high energy photothermal conversion efficiency, which converts light energy into high temperatures of 50 °C or higher after absorption in a short period.[20–23] Several nanomaterials responsive to near-infrared light (NIR) have been developed for aPTT,[24,25] such as carbon nanomaterials,[26] two-dimensional lamellar titanium nanomaterials,[27] gold nanoparticles,[28] and nanoalloys.[29] However, the use of photothermal therapy mediated by nanomaterials with photothermal conversion alone produces local hyperthermia in bacterially infected wounds, which has the potential to increase the toxic effects on normal tissues in the vicinity of the wound. This single-mode photothermal therapy therefore causes irreversible damage to the organism, which is more than worth the cost.[30] Furthermore, heat stimulation activates cellular self-protection mechanisms, such as the synthesis of heat shock proteins (HSPs), which increase tolerance to adverse heat conditions, and the upregulation of HSPs can seriously impair the therapeutic effect of photothermal therapy.[31,32] Therefore, in order to alleviate the stress on photothermal therapy caused by these barriers, mild-temperature photothermal therapy that avoids damage to healthy tissue surrounding the wound shows great potential for clinical application. Still, there is an urgent need to find nanomaterials that can be adapted to mild photothermal sterilization to extend the utility of conventional photothermal therapy.[33,34]

A recent study has shown the interrelationship between ROS and the metabolism of HSPs. ROS storms can effectively disrupt the activity of HSPs,[35] but the required ROS level for mild photothermal potency is not sufficient to disrupt HSP expression at the site of bacterial infection. Hence, maintaining adequate ROS supply levels is the key to this antimicrobial strategy. Since the discovery of magnetite nanoparticles as peroxidase-like enzymes by the team of Yan[36] in 2007, scholars have been focusing their research on nanomaterials with intrinsic enzyme-like activity (nanozymes) for nearly two decades.[37–42] It is a class of materials that exhibit enzymatic catalytic properties that only natural enzymes possess at the nanoscale and has attracted widespread interest due to its high specific surface area, ease of surface modification and functionalization, low cost, high catalytic activity, and biocompatibility. Many peroxidase-like nanozymes that can generate ROS, such as singlet oxygen($_1O^2$), hydroxyl radicals(·OH), and superoxide anions (O^{2-}), have been investigated for antimicrobial therapy based on oxidative stress.[43–47] Among them, palladium-based nanomaterials are promising candidates for antimicrobial applications due to their high biocompatibility,[48] but the design of single-atom nanozymes seems to be thin to enhance the high catalytic activity of palladium nanozymes, especially in the aspect of antibiofilm applications. Many reports have shown that the catalytic activity of single-atom nanozymes can be enhanced by combining with other metals to form alloy nanozymes structures.[49–52] The advantages of good thermal conductivity and low cost of copper[53] could be used to generate more efficient ROS through the synthesis of palladium-copper alloy nanozymes. In this work, we found that palladium-copper nanoparticles (PC-NPs) have nanozyme activity and can catalyze the production of hydroxyl radicals from hydrogen peroxide, and their photothermal conversion properties can be applied to photothermal therapy. Therefore, we wondered whether combining the two characteristics could break through the limitations of single-modality treatment with a programmatic approach. Based on the previous findings, the experiment was designed to first penetrate the bacterial biofilm through the production of PC-NPs-derived active oxygen with the presence of a small amount of hydrogen peroxide. Then, the bacterial biofilm is dispersed to a certain extent. The PC-NPs are subsequently irradiated by a near-infra-red laser, which is highly efficient in photothermal conversion, to achieve a programmed mild photothermal bactericidal treatment that avoids damage to normal tissue.

PC-NPs achieve the combined advances of CDT and PTT in antimicrobial therapy due to their POD-like activity and photothermal conversion efficiency. PC-NPs can effectively catalyze their production of hydroxyl radicals (·OH) in the presence of a relative low level of H_2O_2, leading to the bacteria's oxidative damage. Meanwhile, under 808 nm NIR laser irradiation, they convert light energy into heat energy, which can lyse the bacteria quickly and avoid normal tissue

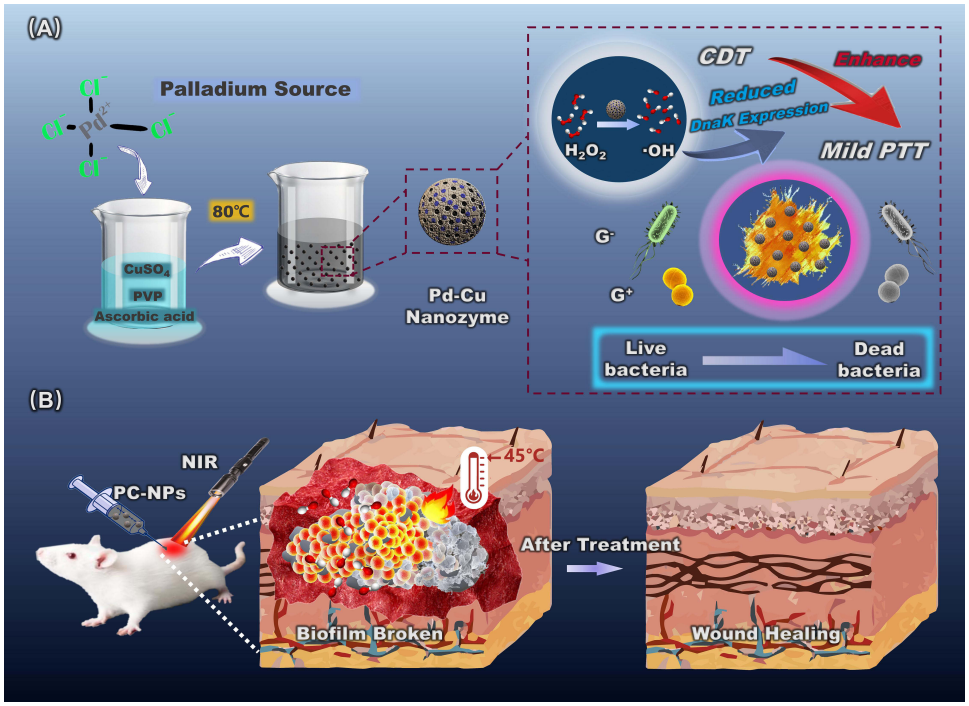

Figure 1 (**A**) Schematic representation of the synthesis and bactericidal effect of palladium-copper nanoparticles (PC-NPs). (**B**) Mechanism of PC-NPs promoting wound healing in bacterial infections of mice.

damage (Figure 1). Therefore, this study was designed to evaluate the photothermal conversion and nanozyme efficacy in killing bacteria in the infection site, as well as reveal the potential mechanism. Firstly, PC-NPs with an average particle size of 4.7 nm were prepared in a one-step method using PVP as a stabilizer and L-ascorbic acid as a reducing agent. Small-sized metal nanospheres have been previously shown to have good enzyme-like activity,[54,55] and the present experiments demonstrate that PC-NPs have good peroxidase-like activity and can catalyze the production of hydroxyl radicals from hydrogen peroxide. They possess the near-infrared light absorption band, which reveals their potential photothermal properties as well. Secondly, it was found that they can down-regulate DnaK protein (a classical Hsp70 homologue of *E. coli*) expression at working concentrations of H_2O_2 by Western Blotting assay (Figure 1A). In vivo antibacterial experiments based on the mouse of bacterially infected wound model showed that the synthesized PC-NPs effectively promoted the healing of bacterially infected wounds, and a series of experiments such as cytotoxicity and histological properties well indicated that they have good biocompatibility (Figure 1B).

Materials and Methods

Reagents and Instruments

Palladium (sodium chloropalladate), copper (copper sulphate), polyvinylpyrrolidone (PVP), crystalline violet, methanol, 3,3',5,5'-tetramethylbenzidine (TMB) and ascorbic acid are from Aladdin Industries Ltd. Other reagents are from Sinopharm Chemical Reagent Co., Ltd. All chemicals were analytical grade reagents. Trypsin soy broth (TSB) and calcein-AM/PI staining kit is provided by Solarbio Science & Technology Co., Ltd. Luria-Bertani (LB) broth are from Sangon Biotech. Fresh human erythrocytes are provided by Hunan Normal University Medical College Hospital. *Staphylococcus aureus* (ATCC12600), *Escherichia coli* (ATCC25922) were preserved in our laboratory. L02 cells were purchased from icell Bioscience (Shanghai, China). DnaK (1:1000, Cusabio Technology, Houston, TX, USA). IgG secondary antibodies (1:10,000; Abclonal technology, Cambridge, MA, USA). Female BALB/c mice (6~8 weeks) were purchased from Slake Jingda Laboratory Animal Co., Ltd. The ultrapure water from a Milli-Q Advantage A10 ultra-pure water system (18.2 MΩ) was used throughout the experiments. The pH of all solutions was calibrated with a San-Xin MP511 miniature pH meter (Shanghai, China). Centrifugation was performed on Beckman Coulter Allegra

25R centrifuge (America). The UV–vis spectrum was measured on an Eppendorf Bio-Spectrometer basic (Eppendorf, Europe; https://www.eppendorf.com/CN-zh/). The transmission electron microscopy (TEM) image was collected on a JEOL-2100 plus transmission electron microscope (JEOL CO., LTD, Japan; https://www.jeol.co.jp).

Synthesis of PC-NPs

PVP powder, L-ascorbic acid and $CuSO_4$-$5H_2O$ powder were added in a ratio of 3:2:1 to a flask containing 30 mL of deionized water. All of these substances are then heated to 80°C by means of a magnetic stirrer, followed by the addition of sodium chloropalladate of 20 mg/mL, at which point the solution changed from blue to black and stirring was continued for three hours. After dialysis, the samples were collected by vacuum freeze-drying and the black product was obtained as PC-NPs.

Photothermal Effect of PC-NPs

The photothermal conversion of PC-NPs were explored under laser irradiation at 808 nm in the near infrared. Firstly, PC-NPs were irradiated at different power densities (0.5 W cm^{-2}, 1 W cm^{-2} and 1.5 W cm^{-2}); afterwards a wide range of PC-NPs solutions from 0 to 300 μgmL^{-1} were prepared and the solution temperature was recorded promptly under the same laser irradiation. Finally, the photothermal stability of PC-NPs (300 $\mu g\ mL^{-1}$) were evaluated by repeating the laser on-off cycle five times. The corresponding photothermal conversion efficiency of PC-NPs was calculated using the heat transfer model established by Roper.

Peroxidase-Like Activity of PC-NPs

The peroxidase-like activity of PC-NPs were assessed by colorimetric analysis using TMB as the oxidase substrate. Briefly, PC-NPs, HAc-NaAc buffer, TMB, and H2O2 were incubated together at room temperature. The UV absorbance of the mixture was measured every 10 minutes by varying the concentration of PC-NPs. In addition, the same concentration of PC-NPs was used to change the pH value of buffer solution, so as to explore the optimal reaction pH of PC-NPs as peroxide-like enzymes. The absorbance changes generated by the above tests are due to the oxidation of TMB into blue oxTMB. Its absorbance values at 650nm were measured under different reaction conditions. Finally the Michaelis constant (Km) and maximum velocity (Vmax) were calculated by fitting the curves of the Michaelis-Menten equation.

In vitro Antibacterial Effect

The in vitro antibacterial effect of PC-NPs with CDT and PTT activity was assessed by plate counting. Bacteria were dispersed and diluted to 10^6 CFU mL^{-1}, which was then added to the PC-NPs solution in a 1:1 ratio. After treatment with or without H_2O_2 (1 mM) and 808 nm laser irradiation (1.5 W cm^{-2}, 12 min), respectively, the mixture was incubated for 1 h. The concentration of bacteria counted on the plate was reduced by two orders of magnitude, and 50 μL were evenly coated on the solid plate to record the number of colonies after overnight.

Fluorescently labelled live/dead bacteria from the different treatment groups were imaged using CLSM. After the bacteria were treated with different treatment groups, 10 μL of Calcein-AM/PI double staining kit and 500 μL of the above bacterial suspension (10^6 CFU mL^{-1}) were co-incubated for 50 minutes in the dark. The bacterial samples after the above process were placed on the surface of slides and observed with a laser confocal microscope.

For further morphological measurements of the bacteria, the bacterial suspensions were washed approximately 10 times with sterile water and then fixed in 2.5% glutaraldehyde at 4 °C for 12 h. To dehydrate the bacterial cells, the samples were treated sequentially with ethanol at concentrations of 30%, 50%, 70%, 80%, 90% and 100% for 5 to 10 min. All bacterial samples were dropped on aluminium sheets and sputter plated for Scanning electron microscopy was performed.

Western Blotting

Equal volumes of bacteria from different treatments as well as the blank group were collected, centrifuged at 10,000rmp for 5min, and the precipitate was washed twice with PBS at a concentration of 0.1M at pH 7.4 and the bacteria were suspended in 1mL of PBS. The bacteria were pulverised using an ultrasonic wall breaker and the sediment was collected

by centrifugation. Adding 1% Protease Inhibitor Cocktail (NCM biotech) to the supernatant and mixing with loading buffer (NCM biotech) followed by boiling at 100°C for 15 min, equal amounts of proteins were separated by 10% SDS-PAGE (Epizyme biotech) and transferred to PVDF membrane (Millipore). 5% BSA was utilized for blocking with 2h. Then, incubate with antibodies against DnaK (1:1000 dilution, Cusabio) and GAPDH (1:10,000 dilution, Abcam) at 4°C for 12 hours. The bands were washed for three times (5 min for each) with TBST and subsequently incubated with HRP-conjugated secondary antibodies (Abclonal) for 1.5h. Finally, the bands were measured by the ChemiDoc XRS+ Imaging system (Bio-Rad) and Image Lab (Bio–Rad) was used for quantifying the relative expression of target proteins.

In vitro Antibacterial Biofilm Activity

The biofilms were formed by co-incubation of bacteria and PC-NPs in 96-well plates. After the bacteria were irradiated and then incubated for 48 h. The generated biofilms were washed twice in 33% acetic acid solution, fixed in methanol and stained with 0.1% crystalline violet for few minutes. Finally, the biofilms were dissolved in 33% acetic acid solution and the UV-Vis absorption spectra were measured at 595 nm to assess the biofilm formation capacity.

To further validate the antibiofilm activity of the PC-NPs nanozymes treatment platform, the bacterial activity within the biofilm was investigated. Bacteria cells were isolated from the formed biofilm by ultrasound machine. The diluted suspension (50 μL) was evenly coated on the solid plate to count the number of colonies after overnight. The differently treatment groups were stained with SYTO9 and imaged with a laser confocal microscope (CLSM). In addition, the morphology of bacteria in the biofilms under different treatment conditions was observed using scanning electron microscopy. In brief, the treated biofilms were washed with water, followed by fixation in methanol for 30 min and natural drying overnight. Finally, the samples were plated and characterized using scanning electron microscopy (SEM).

In vitro Cytotoxicity Test

L02 cells (normal liver cell line) were cultured in RPMI 1640 medium. These cultures were supplemented with 10% fetal bovine serum (FBS), 100 U/mL penicillin and 100 μg/mL streptomycin, and maintained at 37 °C in a 5% CO_2 atmosphere in humidified HF90 CO_2 incubator (Shanghai Lishen Scientific Equipment Co., Ltd.). All of cells used in this study were obtained from the Cell Bank of the Committee on Type Culture Collection of the Chinese Academy of Sciences (Shanghai, China). The cell density was determined by hemocytometer before any cell experiments.

The cytotoxicity of PC-NPs was evaluated using the MTT standard method. Normal liver L02 cells were inoculated in 96-well plates and incubated for 24 h. The medium was removed and the cells were washed with sterile PBS to remove the residual medium. Next, different concentrations of PC-NPs (50–300 μg/mL) were added to the plates and incubation was continued for 12 h. After incubation, 100 μL of fresh cell culture medium and 10 μL of MTT solution were added to each well for another 1 h. The absorbance of each well at 490 nm was recorded using an enzyme marker. As a control, cells untreated with PC-NPs were subjected to the same study. Cell viability was calculated according to the equation: Cell Viability(%)=A /A_0×100%, Where A and A_0 represent the absorbance of the experimental and control groups respectively.

Hemolysis Assays

Fresh blood was centrifuged and washed five times with PBS. The prepared erythrocytes were diluted 20-fold and 300 μL was then incubated with 700 μL of different concentrations of PC-NPs for 4 h. After centrifugation, the supernatant was taken and the absorbance of the supernatant at 495 nm was recorded using an enzyme-labeled instrument. Deionized water and PBS-treated groups were used as positive and negative control groups, respectively. The hemolysis rate was determined by UV spectrophotometry.

In vivo Antibacterial Test

All animal research experimental protocols were approved by the Animal Ethics Committee of Hunan Normal University (20,202–296) and implemented in accordance with the guidelines of the Animal Protection and Utilization Committee of Hunan Normal University. To evaluate the in vivo antibacterial effect of PC-NPs, a series of studies were carried out using a mouse trauma model.

Female Balb/c mice (6–8 weeks) were anaesthetized by intraperitoneal injection of 1% sodium pentobarbital (30 mg kg^{-1}). The back of each mouse was shaved and disinfected with 75% ethanol. All mice were given a prototypical skin wound of approximately 6 mm in diameter and injected subcutaneously with 100 μL of bacteria solution (10^7 CFU mL^{-1}). After 2 days incubation, a trauma infection model was formed on the back of each mouse. The infected mice were randomly divided into 7 groups: PBS, PBS/NIR, H_2O_2, Pd-Cu, Pd-Cu/NIR, Pd-Cu/H_2O_2, Pd-Cu/H_2O_2/NIR. There were no less than 5 mice in each of the above groups. To obtain more accurate in vivo antibacterial data, the experimental conditions were highly consistent across groups, including injection dose (100 μL, 100 μg mL^{-1}), laser power intensity (1.5 W cm^{-2}) and irradiation time (12 min). Real-time temperature changes in mice before and after different treatments were measured with a thermal imager under 808 nm NIR light irradiation. After various treatments, the size of the trauma on the back of the mice was recorded daily. The body weight of each mouse was also measured daily using an electronic scale. After 5 days of treatment, traumatic tissue was taken from the mice and placed in sterile PBS overnight. Samples were then analyzed using the gradient dilution smear method.

At the end of the in vivo antibacterial assay, traumatic tissues of mice were taken for H&E staining to evaluate the anti-infective effect of PC-NPs. The collected tissues were fixed in 10% paraformaldehyde, embedded in paraffin, sectioned and observed by H&E staining.

In vivo Biocompatibility Evaluation

The major organs of the terminally treated mice were collected for histological analysis to further assess the in vivo biosafety of PC-NPs.

Statistical Analysis

All experiments were conducted at least in triplicate. All data were expressed as the mean ± standard deviation and analyzed using one-way analysis of variance (ANOVA) following by a least significant difference (LSD) multiple comparison test. Differences with $^*P < 0.05$, $^{**}P < 0.01$, $^{***}P < 0.001$ were noted as statistically significant.

Results and Discussion

Synthesis and Characterization of Palladium-Copper Nanozymes (PC-NPs)

The PC-NPs were synthesized using a one-step method and were further analyzed using transmission electron microscopy (TEM), X-ray diffraction (XRD), Fourier transform infrared spectroscopy (FTIR), and ultraviolet-visible spectroscopy (UV-Vis) (Figure 2). Transmission electron microscopy results indicated that the prepared PC-NPs were homogeneous and uniformly spherical with an average particle size of about 4.7 nm (Figure 2A). EDS elemental mapping analysis plots showed that Pd, Cu, C, N, and O were distributed in PC-NPs (Figure 2B). X-ray diffraction results showed that PC-NPs had multiple diffraction peaks at 30–90°, indicating that PC-NPs had a crystalline structure (Figure 2C). FTIR analyzed the intermolecular interactions between PC-NPs and PVP. PVP has an absorption band at 1600–1700 cm^{-1} corresponding to the C=O functional group, and FTIR spectra measured after the synthesis of PC-NPs showed the same characteristic peak absorption band, demonstrating the indelible role of PVP as a stabilizing agent in the synthesis of PC-NPs (Figure 2D). PC-NPs have a broad absorption band in the UV-Vis spectrum from the visible to the near-infrared region, suggesting that they may have the potential to convert near-infrared light to thermal energy, which will provide a viable basis for subsequent evaluation of the PTT bactericidal efficacy of PC-NPs (Figure 2E).

Photothermal Properties

To analyze the photothermal properties of the PC-NP for antimicrobial PTT therapy (Figure 3), the PC-NPs evaluation was started with temperature detection under different concentrations of PC-NPs and laser power from an 808 nm NIR laser. The results show that PC-NPs warm up with increasing irradiation time and the temperature increased with the elevated laser power under PC-NPs concentration of (300 μg mL^{-1}), as well as the increased PC-NPs concentration (Figure 3A and B). All of the warming curves were positively correlated with PC-NPs concentration and laser power. Ultrapure water was used as a control group and exposed to the 808 nm laser at the selected power with a temperature

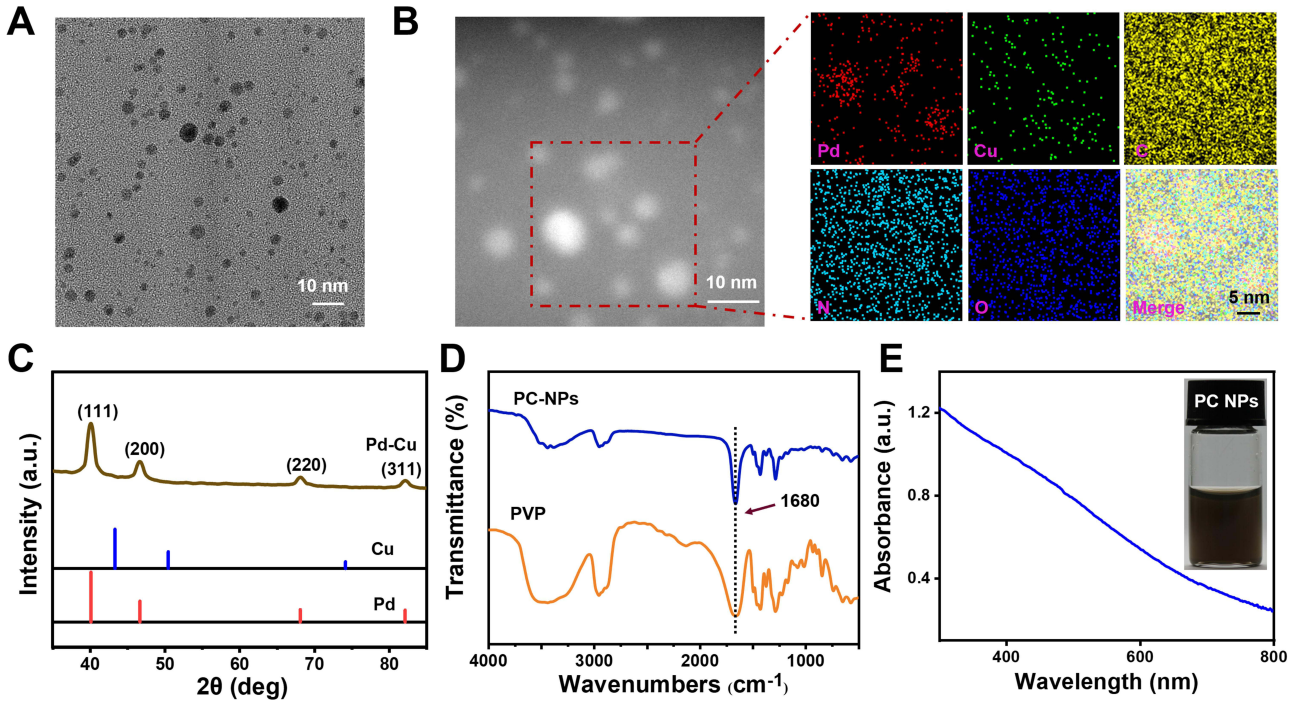

Figure 2 Characterization of PC-NPs. (**A**) TEM images. (**B**) TEM Element Mapping images of Pd and Cu.(**C**) XRD pattern. (**D**) FTIR spectra. (**E**) UV−vis absorption spectrum of PC-NPs, the inset is the digital image.

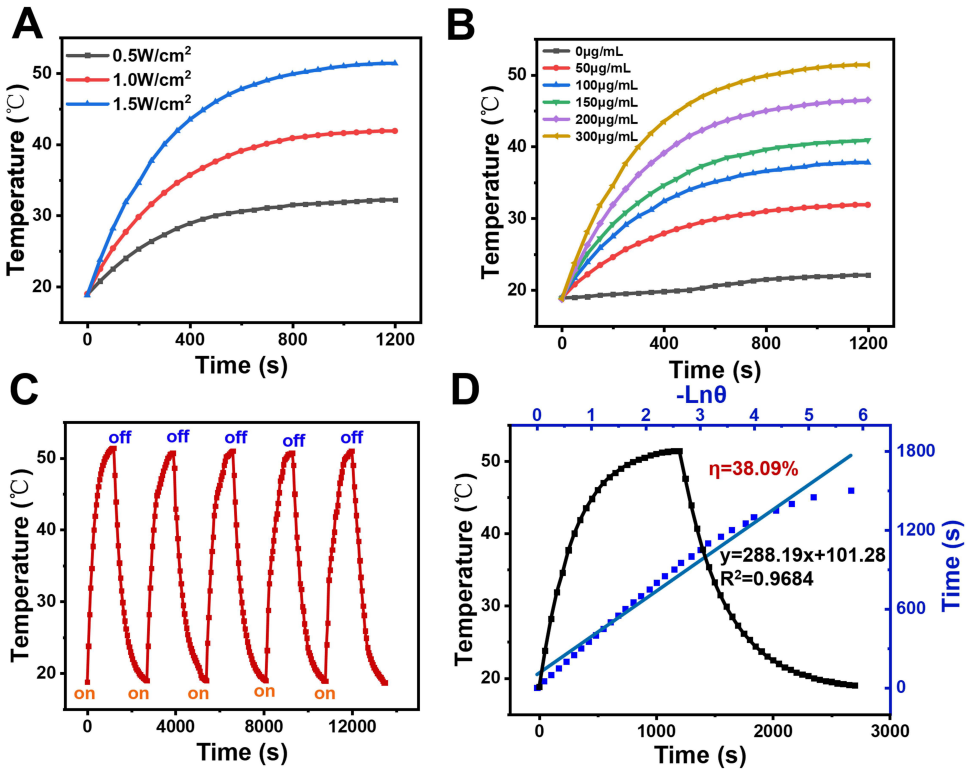

Figure 3 Photothermal properties of PC-NPs. (**A**) Temperature changes of PC-NPs with different power densities. (**B**) Concentration-dependent temperature changes of PC-NPs under 808 nm laser irradiation. (**C**) Temperature changes of PC-NPs (80 μg mL^{-1}) during five "on/off" cycles of laser irradiation (1.5 W cm^{-2}). (**D**) Temperature change curves of PC-NPs undergoing the laser "on-off" process, as well as cooling times and -lnθ from PC-NPs with NIR laser off were obtained as linear fit curves to calculate the photothermal conversion efficiency (η).

change of approximately 3 °C. In addition, no significant change in PC-NPs' photothermal performance was observed when subjected to five cycles of laser "on and off" cycles (Figure 3C). In order to calculate their photothermal conversion efficiency, the PC-NPs were warmed to a stable temperature, and then cooled to the initial temperature. The warming and cooling curves were plotted under an "on-off" cycle to determine the photothermal conversion efficiency (η). The calculated η was 38.09%, consistent with the expected good photothermal conversion performance of PC-NPs (Figure 3D). Shortly, PC-NPs exhibited good photothermal properties for subsequent antimicrobial treatment.

Peroxidase-Like (POD) Activity

Apart from the photothermal properties of PC-NPs, their peroxide-like activity was also evaluated. PC-NPs were probed using 3.3',5,5'-tetramethylbenzidine (TMB) as the catalytic substrate, and the production of ·OH was further probed using 5.5-dimethyl-1-pyrroline-N-oxide (DMPO) (Figure 4D). In the presence of H2O2, PC-NPs could catalyze the oxidation of TMB to form blue oxTMB, as evidenced by the characteristic peak at 650 nm in the UV absorption spectrogram (Figure 4A). In the presence of PC-NPs, H2O2, and DMPO, a 1:2:2:1 electron spin resonance (ESR) signal was observed, which is the signature signal peak of PC-NPs as the peroxidase class, indicating the production of ·OH from H_2O_2 (Figure 4B). The characteristic absorption peak of TMB at 650 nm increased with time and, in addition, the intensity of the absorption peak of oxTMB was found to be similar to that of PC-NPs and H_2O_2 concentrations, showing a clear positive correlation effect (Figure 4C, D and E). As shown, the Michaelis constant (Km) and the maximum reaction rate (Vmax) of PC-NPs at room temperature (25 °C) were 0.97 mM and 1.773×10^{-7} m s^{-1}, respectively, which indicated that PC-NPs had good catalytic activity at room temperature (25 °C) (Figure 4F).

In addition to optimizing the reaction conditions such as reaction time, PC-NPs, and H_2O_2 concentration, the pH condition also requires optimization as PC-NPs exhibit pH-dependent peroxidase-like properties and have significant catalytic activity only in a slightly acidic environment. Since the bacterial infection site is slightly acidic (pH 5.0–5.5), the PC-NPs can mimic the bactericidal effects of·OH produced by its peroxidase-like activity with a relatively low level

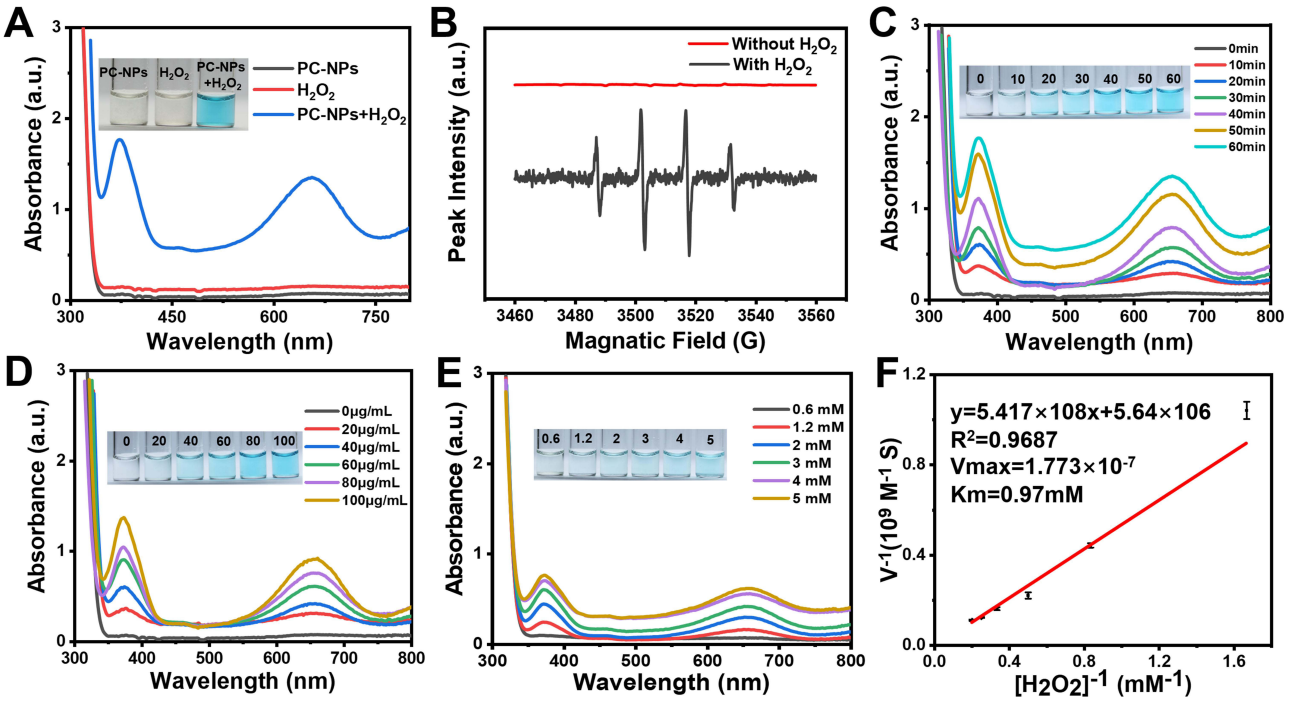

Figure 4 Peroxidase-like activity of PC-NPs. (**A**) Absorption changes of TMB in the presence of PC-NPs and H_2O_2. (**B**) ESR spectra of DMPO-OH adducts. (**C**) Time-dependent absorption changes of TMB in the presence of PC-NPs and H_2O_2. PC-NPs concentration-dependent (**D**) and H_2O_2 concentration-dependent (**E**) results of the TMB chromogenic reaction. The corresponding concentrations of TMB was 0.25 mM. (**F**) Double-reciprocal plot for determining the kinetic constants of PC-NPs for H_2O_2 as the substrate.

of H_2O_2 (Figure S1). Thus, the above experiments demonstrate the excellent catalytic efficiency of PC-NPs as peroxidase-like enzymes.

In vitro Antibacterial Activity

The inhibitory effect of PC-NPs on the growth of *Staphylococcus aureus* (G^+) and *Escherichia coli* (G^-) was assessed through a series of experiments. Firstly, the bacterial smear plates from the different treatment groups were quantified and analyzed. As shown in Figure 5A–D, the treatment measures of NIR light and H_2O_2 alone did not inhibit bacterial growth by more than 25%. Compared to *S. aureus, E. coli* was less susceptible to PC-NPs, but there was little difference in the effect of NIR light on the growth of these two bacteria. The PC-NPs/H_2O_2 treatment group exhibited increased ROS bactericidal efficacy compared to PC-NPs treatment alone. To integrate the photothermal conversion and peroxidase-like activity of PC-NPs, a further photothermal treatment group with exposure to NIR light reduced the relative bacteria viability of *S. aureus* and *E. coli* to 3.8% and 0.7%, respectively. Therefore, it is evident that the combination of PC-NPs-based CDT and PTT is feasible and efficient for the treatment of bacterial infections.

Next, the staining images of live/dead bacteria after different treatments were captured by laser confocal microscopy (CLSM). In this case, live bacteria were labeled with Calcein-AM (green fluorescence), and dead bacteria were labeled

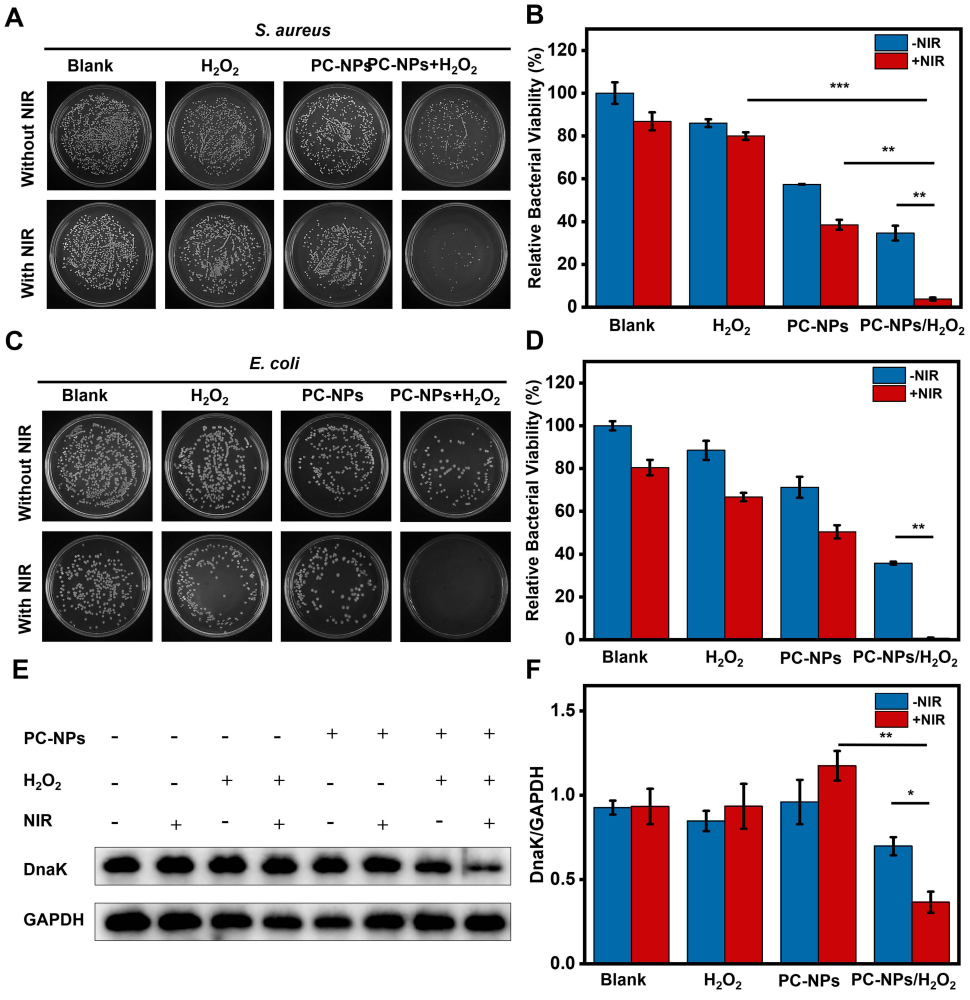

Figure 5 In vitro antibacterial activity of PC-NPs. (**A**) Photographs of bacteria colonies formed by *S. aureus* after exposure to PBS, H_2O_2 (1 mM), PC-NPs (100 μg mL^{-1}), and PC-NPs + H_2O_2 after 12 min with/without laser irradiation (1.5 W cm^{-2}). (**B**) The corresponding bacterial viability rates of *S. aureus*. (**C**) Photographs of bacteria colonies formed by *E. coli* after exposure to PBS, H_2O_2 (1 mM), PC-NPs (100 μg mL^{-1}), and PC-NPs + H_2O_2 after 12 min with/without laser irradiation (1.5 W cm^{-2}). (**D**) The corresponding bacterial viability rates of *E. coli*. (**E**) Western blotting images of DnaK after different treatments. (**F**) DnaK/ GAPDH gray value ratios obtained from Western blotting. Data are expressed as mean ± S.D., n = 3, *p < 0.05, ** p< 0.01, ***p< 0.001.

with PI (red fluorescence) (Figure S2). The blank control showed green fluorescence throughout the field of view, while no red fluorescence was observed. The H_2O_2 and PC-NPs treated groups had visible red fluorescence with scattered green fluorescence, and no green fluorescence was observed, demonstrating that the bacteria were dead.

Finally, the morphology of all treated bacteria was captured by scanning electron microscopy (SEM). As shown in Figure S3, the surfaces of the bacteria in the blank control and H_2O_2 groups were smooth and intact with or without NIR laser irradiation, indicating that PC-NPs had little effect on the integrity of the bacterial cells. In contrast, the integrity of the bacteria was significantly damaged in the PC-NPs/NIR and PC-NPs /H_2O_2 treated groups. These bacteria-killing effects were attributed to the dual action of heat and ·OH. Consistent with the effects of previous experiments, the combination of PTT and CDT had the most pronounced treatment effect on bacteria, with cytoplasmic release and fragmentation of most bacteria observed.

Western-Blotting Test to Investigate the Effect of Different Treatment Groups on DnaK Protein

The expression of heat shock proteins is the main reason for PTT tolerance. As DnaK is a classical Hsp70 homologue of *E. coli*, we tested the relationship between the PC-NPs composite anti-bactericidal platform and DnaK expression under different spatiotemporal conditions, by setting up a total of eight treatment groups with PBS, H_2O_2, PC-NPs and PC-NPs/H_2O_2 with or without NIR light (Figure 5E and F, uncropped Western blotting image was provided in Figure S4). The results showed that H_2O_2 and NIR did not fluctuate the expression of DnaK in the absence of PC-NPs. Through the photothermal conversion of PC-NPs, DnaK expression was up-regulated under the high-temperature conditions generated by NIR-illuminated PC-NPs. Under the treatment of PC-NPs/H_2O_2, the expression of DnaK was greatly inhibited, suggesting that the PC-NP-derived ROS repressed the expression of DnaK. Therefore, in the next step, the PC-NPs/H_2O_2 -treated bacteria were then exposed to NIR light, and the results revealed that the PC-NPs/H_2O_2/NIR-treated group showed lower DnaK expression than the PC-NPs/H_2O_2-treated group. This suggests that NIR light further inhibited the expression of DnaK disrupted by ROS. Therefore, the programmed bactericidal strategy of oxidative stress damage followed by NIR photothermal treatment with PC-NPs was expected to improve PTT bactericidal efficacy, and this process could be carried out under mild PTT conditions.

In vitro Anti-Biofilm Activity

Biofilm formation increases bacterial resistance to antibiotics, and new antimicrobial strategies need to be developed to inhibit the growth of biofilms. We assessed the inhibitory effect of PC-NPs on bacterial biofilm formation and quantified biofilms stained with crystalline violet. As shown in Figure 6A and C, the control groups exhibited higher biofilm density. In the absence of NIR, H_2O_2 and PC-NPs presented some anti-biofilm effects. In contrast, the PC-NPs/H_2O_2/NIR treated group under NIR laser irradiation shows a significant anti-biofilm effect of 85% (Figure 6B) and 93% (Figure 6D) on both G^+ and G^- bacteria growth, respectively. In addition, to show the bactericidal effect of the PC-NPs nanocomposite platform on bacteria deep in the biofilm, the survival rate of bacteria in the biofilm was examined by the plate count method. The bacteria were isolated by ultrasonic shaking, and the biofilms from different treatments were subjected to plate counting. As shown in Figure S5, only about 10% of *S. aureus* and 5% of *E. coli* remained in the biofilm of the PC-NPs/H_2O_2/NIR treatment group. Afterward, the status of the SYTO9-stained biofilms was observed in a three-dimensional mode using laser confocal microscopy (CLSM) (Figure 6E). The biofilm of the control was flat and of uniform thickness, whereas the biofilm treated with PC-NPs/H_2O_2/NIR showed a very thin green color in the field of view, which proved that the biofilm was severely fragmented and its thickness was substantially reduced. Finally, the states of the bacterial biofilms after different treatments were photographed using a scanning electron microscope (Figure S6). Consistent with the results of the CLSM experiments, little biofilm was left after treatment with PC-NPs/H_2O_2/NIR. These demonstrated that the programmed CDT/PTT antibacterial strategy based on PC-NPs is effective and performs well in inhibiting biofilm formation.

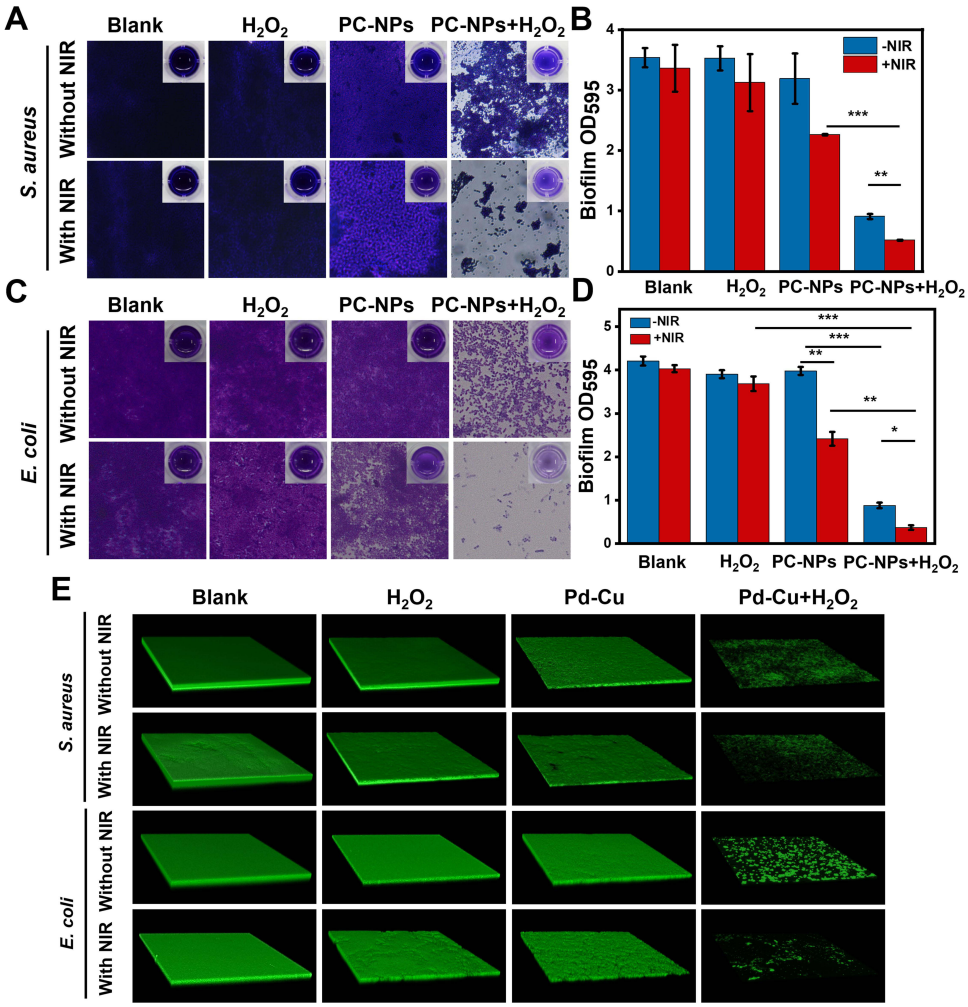

Figure 6 In vitro anti-biofilm activity of PC-NPs. (**A**) Microscopy images of *S. aureus* biofilms and *E. coli* biofilms (**C**) stained with crystal violet after various treatments. Inset: The corresponding digital photographs of biofilms formed in 96-well plates. (**B**) UV–vis absorption intensities at 595 nm of *S. aureus* biofilms and *E. coli* biofilms (**D**) stained with the crystal violet. Data are expressed as mean ± S.D., n = 3, *p < 0.05, **p < 0.01, ***p< 0.001. (**E**) 3D CLSM images (212.5 × 212.5 μm) of biofilms with various treatments.

In vivo Antibacterial Activity

Investigation of PC-NPs' biocompatibility is a prerequisite for their application on mouse wound infection models. Therefore, we assessed the biocompatibility of PC-NPs by MTT cytotoxicity assay and hemolysis assay. First, the potential cytotoxic effect of PC-NPs on L02 cells was examined using. As displayed in Figure S7A, the survival rate of L02 cells was not significantly affected after 24 h treatment with PC-NPs (0–300 μg mL^{-1}). Second, the effect of PC-NPs on erythrocytes was investigated using the hemolysis properties of erythrocytes. The supernatant of the water-treated group (positive control) was bright red, whereas the supernatant of the PBS-treated group (negative control) and different concentrations of the PC-NPs-treated group were colourless and their hemolysis properties were not obvious (Figure S7B). Combining the results of these two experiments, it is not difficult to conclude that PC-NPs have good biocompatibility.

We further explored the role of PC-NPs in the treatment of traumatic infections given its good in vitro antibacterial, anti-biofilm, and low cytotoxic properties. *S. aureus* is a common pathogenic bacterium closely associated with traumatic bacterial infections as well as biofilm-associated infections of medical indwelling devices. Therefore, we evaluated the therapeutic efficacy of the PC-NPs/H_2O_2/NIR nanocomposite platform for traumatic infections by establishing a mouse model of *S. aureus* biofilm infection. The experimental protocol for in vivo antimicrobial biofilm treatment in animals is shown in Figure 7A. *S. aureus* (1×10^7 CFU/mL) was injected into a dorsal wound (approximately 6 mm in diameter) in mice, and the wound model of biofilm infection was formed two days after infection. Temperature changes in wounds of

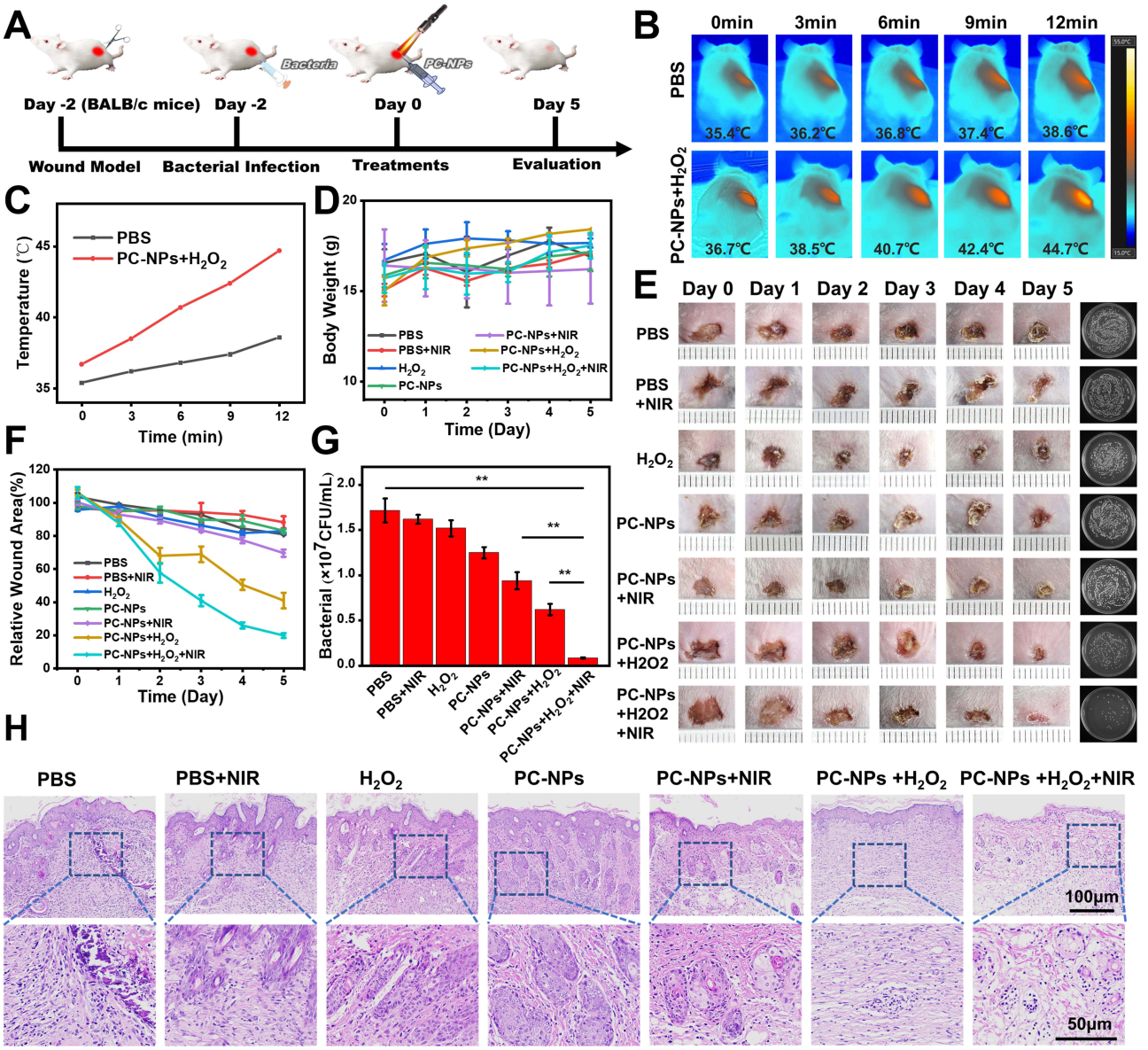

Figure 7 In vivo antibacterial activity of PC-NPs. (**A**) Schematic illustration for the establishment of an in vivo biofilm-infected wound model and the subsequent treatment regime. (**B** and **C**) Thermal images of mice under NIR irradiation and the corresponding photothermal heating curves. (**D**) Body weight changes of mice with various treatments. (**E** and **F**) Digital photos of biofilm-infected wounds and corresponding quantitative analysis of relative wound area. (**G**) Bacteria colonies of infected wound tissues after different treatments for 7 days. Data are expressed as mean ± S.D, n = 3, **p < 0.01. (**H**) H&E staining of tissue slices of the infected wounds on mice after various treatments.

mice treated with PBS or PC-NPs/H_2O_2 were recorded by thermography under NIR exposure (Figure 7B). After 12 minutes of irradiation, the temperature increased from 36.7 °C to 44.7 °C, whereas the temperature of PBS-treated group increased by only 3 °C during the same time (Figure 7C).

Mice infected with bacterial biofilm were divided into the following seven treatment groups: PBS, PBS/NIR, H_2O_2, PC-NPs, PC-NPs/NIR, PC-NPs/H_2O_2, and PC-NPs/H_2O_2/NIR. In order to obtain accurate data, the experimental conditions in each group were highly consistent. During the experiment, the body weight and wound size of the mice were recorded daily. The body weights of mice in all seven groups remained within a reasonable range (14–19 g), indicating that there were no significant side effects in vivo was caused. However, wound healing trends differed between treatment groups. Digital photographs of the mice wounds among groups visually show the change in size over time (Figure 7D). The mice in the PC-NPs/ H_2O_2/NIR group showed the best wound healing results, proving that the PC-NPs/

H_2O_2/NIR composite nanoplatform has a good antibacterial biofilm effect (Figure 7E). Subsequently, a series of quantitative measurements of the corresponding wounds in each group were performed and recorded (Figure 7F). Wound healing was poorer in the H_2O_2 and PC-NPs groups compared to the PBS control group. For the PC-NPs/NIR group, wound healing and wound crusting processes were both relatively slower, although wound crusting occurred after NIR laser irradiation. As Figure 7 shows, PC-NPs/H_2O_2 also had some effects on wound healing promotion, but not ideally. The PC-NPs/H_2O_2/NIR group had the best wound healing performance regarding both wound healing speed and wound size. At the end of the treatment, wound tissue was collected for bacterial counting (Figure 7G). The total bacterial colony count in the PC-NPs/H_2O_2/NIR treated group decreased to 4.9% of that in the PBS control group.

Histological analysis of wound sections using hematoxylin-eosin (H&E) staining was performed further to assess the healing of infected wounds after different treatments. As shown in Figure 7H, there was a clear inflammatory response (blue) on the biofilm-infected wounds in the groups treated with PBS, H_2O_2 and PC-NPs. In contrast, inflammatory cells at the infection site were significantly reduced in the PC-NPs/H_2O_2/NIR group. It was well indicated that a programmed combination therapy platform based on CDT and PTT with PC-NPs nanoparticles is promising for the treatment of traumatic biofilm infections.

In addition, H&E staining was performed on the major organs (heart, liver, spleen, lung and kidney) of the mice treated with PBS and PC-NPs/H_2O_2/NIR (Figure S8). No significant abnormalities were found in the organs of the PC-NPs/H_2O_2/NIR-treated mice compared to the PBS control group. With these benefits, the established CDT and PTT-based PC-NPs platforms hold promise to meet future demands for safe, simple to use, highly effective in vivo antibacterial and anti-biofilm.

Conclusion

In this study, we have successfully constructed a programmed therapeutic platform that produces ROS to down-regulate heat shock proteins from alloy nanozymes with peroxidase-like activity, thereby reducing bacterial stress response to high temperatures and increasing mild photothermal therapy efficacy in bacterial biofilm-infected wounds. The bactericidal efficacy of this ultra-small PC-NPs nanocomposite is mainly presented by a dual antibacterial mode of CDT and PTT, which exhibits peroxidase-like activity and photothermal conversion capability, respectively. In the presence of imposed hydrogen peroxide, the PC-NPs could generate ROS (·OH), and the generated ROS activates the cleavage of heat shock proteins, ultimately facilitating the efficacy of photothermal antimicrobial therapy (aPTT) in the form of mild photothermal therapy. The constructed system has a higher photothermal conversion efficiency (38.09%) than common bactericidal nanomaterials. Furthermore, in-vivo anti-biofilm infection experiments provided strong evidence that the PC-NPs dual-mode antimicrobial strategy has significant anti-biofilm properties, shedding light on the elimination of biofilms growing on adherent retention devices. In summary, the ROS-triggered PC-NPs nanozyme mild-temperature photothermal programmed therapy platform provides the basis for the application of the anti-HRP ROS therapy, as well as for the future clinical treatment of biofilm-associated infections.

Acknowledgments

This work was supported by the research grants from National Natural Science Foundation of China (Grant No. 81871577 and No.82272508), and Changsha Municipal Natural Science Foundation (Grant No. kq2202148).

Disclosure

The authors report no conflicts of interest in this work.

References

1. Culyba MJ, Van Tyne D. Bacterial evolution during human infection: adapt and live or adapt and die. *PLoS Pathog*. 2021;17(9):e1009872. doi:10.1371/journal.ppat.1009872
2. Deusenbery C, Wang Y, Shukla A. Recent innovations in bacterial infection detection and treatment. *ACS Infect Dis*. 2021;7(4):695–720. doi:10.1021/acsinfecdis.0c00890
3. Liu S, Lu H, Zhang S, Shi Y, Chen Q. Phages against pathogenic bacterial biofilms and biofilm-based infections: a review. *Pharmaceutics*. 2022;14:2.

4. Wright AJ, Wilkowske CJ. The penicillins. *Mayo Clin Proc*. 1991;66(10):1047–1063. doi:10.1016/s0025-6196(12)61730-3
5. Wilhelm MP. Vancomycin. *Mayo Clin Proc*. 1991;66(11):1165–1170. doi:10.1016/s0025-6196(12)65799-1
6. Davies J, Davies D. Origins and evolution of antibiotic resistance. *Microbiol Mol Biol Rev*. 2010;74(3):417–433. doi:10.1128/mmbr.00016-10
7. Mah TF. Giving antibiotics an assist. *Science*. 2021;372(6547):1153. doi:10.1126/science.abj3062
8. Chellat MF, Raguž L, Riedl R. Targeting Antibiotic Resistance. *Angew Chem Int Ed Engl*. 2016;55(23):6600–6626. doi:10.1002/anie.201506818
9. Hou J, Long X, Wang X, et al. Global trend of antimicrobial resistance in common bacterial pathogens in response to antibiotic consumption. *J Hazard Mater*. 2023;442:130042. doi:10.1016/j.jhazmat.2022.130042
10. Monnier AA, Schouten J, Tebano G, et al. Ensuring antibiotic development, equitable availability, and responsible use of effective antibiotics: recommendations for multisectoral action. *Clin Infect Dis*. 2019;68(11):1952–1959. doi:10.1093/cid/ciy824
11. Flemming HC, Wingender J, Szewzyk U, Steinberg P, Rice SA, Kjelleberg S. Biofilms: an emergent form of bacterial life. *Nat Rev Microbiol*. 2016;14(9):563–575. doi:10.1038/nrmicro.2016.94
12. Liu Y, Li Y, Shi L. Controlled drug delivery systems in eradicating bacterial biofilm-associated infections. *J Control Release*. 2021;329:1102–1116. doi:10.1016/j.jconrel.2020.10.038
13. Beroz F, Yan J, Sabass B, et al. Verticalization of bacterial biofilms. *Nat Phys*. 2018;14(9):954–960. doi:10.1038/s41567-018-0170-4
14. Mutalik C, Okoro G, Chou H-L, et al. Phase-dependent 1T/2H-MoS2 nanosheets for effective photothermal killing of bacteria. *ACS Sustain Chem Eng*. 2022;10(27):8949–8957. doi:10.1021/acssuschemeng.2c02457
15. Mutalik C, Okoro G, Krisnawati DI, et al. Copper sulfide with morphology-dependent photodynamic and photothermal antibacterial activities. *J Colloid Interface Sci*. 2022;607(Pt 2):1825–1835. doi:10.1016/j.jcis.2021.10.019
16. Yougbaré S, Mutalik C, Krisnawati DI, et al. Nanomaterials for the photothermal killing of bacteria. *Nanomaterials*. 2020;10(6):1123. doi:10.3390/nano10061123
17. Yougbaré S, Mutalik C, Okoro G, et al. Emerging trends in nanomaterials for antibacterial applications. *Int J Nanomedicine*. 2021;16:5831–5867. doi:10.2147/ijn.S328767
18. Huo J, Jia Q, Huang H, et al. Emerging photothermal-derived multimodal synergistic therapy in combating bacterial infections. *Chem Soc Rev*. 2021;50(15):8762–8789. doi:10.1039/d1cs00074h
19. Ye Y, Zheng L, Wu T, et al. Size-dependent modulation of polydopamine nanospheres on smart nanoprobes for detection of pathogenic bacteria at single-cell level and imaging-guided photothermal bactericidal activity. *ACS Appl Mater Interfaces*. 2020;12(31):35626–35637. doi:10.1021/acsami.0c07784
20. Zou Y, Zhang Y, Yu Q, Chen H. Photothermal bactericidal surfaces: killing bacteria using light instead of biocides. *Biomater Sci*. 2021;9(1):10–22. doi:10.1039/d0bm00617c
21. Chen J, Ning C, Zhou Z, et al. Nanomaterials as photothermal therapeutic agents. *Prog Mater Sci*. 2019;99:1–26. doi:10.1016/j.pmatsci.2018.07.005
22. Wu H, Song L, Chen L, et al. Injectable thermosensitive magnetic nanoemulsion hydrogel for multimodal-imaging-guided accurate thermoablative cancer therapy. *Nanoscale*. 2017;9(42):16175–16182. doi:10.1039/c7nr02858j
23. Yu K, Liang B, Zheng Y, et al. PMMA-Fe(3)O(4) for internal mechanical support and magnetic thermal ablation of bone tumors. *Theranostics*. 2019;9(14):4192–4207. doi:10.7150/thno.34157
24. Xu JW, Yao K, Xu ZK. Nanomaterials with a photothermal effect for antibacterial activities: an overview. *Nanoscale*. 2019;11(18):8680–8691. doi:10.1039/c9nr01833f
25. Chen Y, Gao Y, Chen Y, Liu L, Mo A, Peng Q. Nanomaterials-based photothermal therapy and its potentials in antibacterial treatment. *J Control Release*. 2020;328:251–262. doi:10.1016/j.jconrel.2020.08.055
26. Xin Q, Shah H, Nawaz A, et al. Antibacterial Carbon-Based Nanomaterials. *Adv Mater*. 2019;31(45):e1804838. doi:10.1002/adma.201804838
27. Rasool K, Helal M, Ali A, Ren CE, Gogotsi Y, Mahmoud KA. Antibacterial Activity of Ti□C□Tx MXene. *ACS Nano*. 2016;10(3):3674–3684. doi:10.1021/acsnano.6b00181
28. Cheeseman S, Christofferson AJ, Kariuki R, et al. Antimicrobial metal nanomaterials: from passive to stimuli-activated applications. *Adv Sci*. 2020;7(10):1902913. doi:10.1002/advs.201902913
29. Fan X, Yahia L, Sacher E. Antimicrobial properties of the Ag, Cu nanoparticle system. *Biology*. 2021;10:2.
30. Hu D, Zou L, Li B, Hu M, Ye W, Ji J. Photothermal killing of methicillin-resistant staphylococcus aureus by bacteria-targeted polydopamine nanoparticles with nano-localized hyperpyrexia. *ACS Biomater Sci Eng*. 2019;5(10):5169–5179. doi:10.1021/acsbiomaterials.9b01173
31. Liberek K, Georgopoulos C. Autoregulation of the Escherichia coli heat shock response by the DnaK and DnaJ heat shock proteins. *Proc Natl Acad Sci USA*. 1993;90(23):11019–11023. doi:10.1073/pnas.90.23.11019
32. Zhang X, Yu W. Heat shock proteins and viral infection. *Front Immunol*. 2022;13:947789. doi:10.3389/fimmu.2022.947789
33. Zhang Y, Wu H, Li P, Liu W, Zhang Y, Dong A. Dual-light-triggered in situ structure and function regulation of injectable hydrogels for high-efficient anti-infective wound therapy. *Adv Healthc Mater*. 2022;11(1):e2101722. doi:10.1002/adhm.202101722
34. Xiong YH, Zhang L, Xiu Z, Yu B, Duan S, Xu FJ. Derma-like antibacterial polysaccharide gel dressings for wound care. *Acta Biomater*. 2022;148:119–132. doi:10.1016/j.actbio.2022.06.018
35. Chang M, Hou Z, Wang M, et al. Cu single atom nanozyme based high-efficiency mild photothermal therapy through cellular metabolic regulation. *Angew Chem Int Ed Engl*. 2022;61(50):e202209245. doi:10.1002/anie.202209245
36. Gao L, Zhuang J, Nie L, et al. Intrinsic peroxidase-like activity of ferromagnetic nanoparticles. *Nat Nanotechnol*. 2007;2(9):577–583. doi:10.1038/nnano.2007.260
37. Huang Y, Ren J, Qu X. Nanozymes: classification, catalytic mechanisms, activity regulation, and applications. *Chem Rev*. 2019;119(6):4357–4412. doi:10.1021/acs.chemrev.8b00672
38. Fedeli S, Im J, Gopalakrishnan S, et al. Nanomaterial-based bioorthogonal nanozymes for biological applications. *Chem Soc Rev*. 2021;50(24):13467–13480. doi:10.1039/d0cs00659a
39. Ouyang Y, O'Hagan MP, Willner I. Functional catalytic nanoparticles (nanozymes) for sensing. *Biosens Bioelectron*. 2022;218:114768. doi:10.1016/j.bios.2022.114768
40. Mou X, Wu Q, Zhang Z, et al. Nanozymes for regenerative medicine. *Small Methods*. 2022;6(11):e2200997. doi:10.1002/smtd.202200997

41. Wu J, Wang X, Wang Q, et al. Nanomaterials with enzyme-like characteristics (nanozymes): next-generation artificial enzymes (II). *Chem Soc Rev*. 2019;48(4):1004–1076. doi:10.1039/c8cs00457a
42. Jiang D, Ni D, Rosenkrans ZT, Huang P, Yan X, Cai W. Nanozyme: new horizons for responsive biomedical applications. *Chem Soc Rev*. 2019;48(14):3683–3704. doi:10.1039/c8cs00718g
43. Song N, Yu Y, Zhang Y, et al. Bioinspired hierarchical self-assembled nanozyme for efficient antibacterial treatment. *Adv Mater*. 2023:e2210455. doi:10.1002/adma.202210455
44. Wang Q, Jiang J, Gao L. Catalytic antimicrobial therapy using nanozymes. *Wiley Interdiscip Rev Nanomed Nanobiotechnol*. 2022;14(2):e1769. doi:10.1002/wnan.1769
45. Azharuddin M, Zhu GH, Das D, et al. A repertoire of biomedical applications of noble metal nanoparticles. *Chem Commun*. 2019;55(49):6964–6996. doi:10.1039/c9cc01741k
46. Ding X, Zhao Z, Zhang Y, Duan M, Liu C, Xu Y. Activity regulating strategies of nanozymes for biomedical applications. *Small*. 2023;19(11):e2207142. doi:10.1002/smll.202207142
47. Chen J, Ma Q, Li M, et al. Glucose-oxidase like catalytic mechanism of noble metal nanozymes. *Nat Commun*. 2021;12(1):3375. doi:10.1038/s41467-021-23737-1
48. Pedone D, Moglianetti M, De Luca E, Bardi G, Pompa PP. Platinum nanoparticles in nanobiomedicine. *Chem Soc Rev*. 2017;46(16):4951–4975. doi:10.1039/c7cs00152e
49. Klębowski B, Depciuch J, Parlińska-Wojtan M, Baran J. Applications of noble metal-based nanoparticles in medicine. *Int J Mol Sci*. 2018;19(12):4031. doi:10.3390/ijms19124031
50. Ali S, Sharma AS, Ahmad W, et al. Noble metals based bimetallic and trimetallic nanoparticles: controlled synthesis, antimicrobial and anticancer applications. *Crit Rev Anal Chem*. 2021;51(5):454–481. doi:10.1080/10408347.2020.1743964
51. Loza K, Heggen M, Epple M. Synthesis, structure, properties, and applications of bimetallic nanoparticles of noble metals. *Adv Funct Mater*. 2020;30(21):1909260. doi:10.1002/adfm.201909260
52. Cai T, Fang G, Tian X, Yin JJ, Chen C, Ge C. Optimization of antibacterial efficacy of noble-metal-based core-shell nanostructures and effect of natural organic matter. *ACS Nano*. 2019;13(11):12694–12702. doi:10.1021/acsnano.9b04366
53. Ermini ML, Voliani V. Antimicrobial nano-agents: the copper age. *ACS Nano*. 2021;15(4):6008–6029. doi:10.1021/acsnano.0c10756
54. Jiang X, Du B, Huang Y, Zheng J. Ultrasmall noble metal nanoparticles: breakthroughs and biomedical implications. *Nano Today*. 2018;21:106–125. doi:10.1016/j.nantod.2018.06.006
55. Zhang S, Lu Q, Wang F, et al. Gold-platinum nanodots with high-peroxidase-like activity and photothermal conversion efficiency for antibacterial therapy. *ACS Appl Mater Interfaces*. 2021;13(31):37535–37544. doi:10.1021/acsami.1c10600